

Ocean dynamics of outer solar system satellites

K. M. Soderlund¹

¹Institute for Geophysics, Jackson School of Geosciences, The University of Texas at Austin, Austin,
Texas, USA

Key Points:

- Ocean dynamics are important for the habitability of icy ocean worlds.
- Strong ocean currents likely exist in Enceladus, Titan, Europa, and Ganymede.
- Convective heat transfer in the ocean varies with latitude and may modify the thermophysical structure of the ice shell.

arXiv:1901.04093v1 [physics.geo-ph] 14 Jan 2019

Abstract

Ocean worlds are prevalent in the solar system. Focusing on Enceladus, Titan, Europa, and Ganymede, I use rotating convection theory and numerical simulations to predict ocean currents and the potential for ice-ocean coupling. When the influence of rotation is relatively strong, the oceans have multiple zonal jets, axial convective motions, and most efficient heat transfer at high latitudes. This regime is most relevant to Enceladus and possibly to Titan, and may help explain their long-wavelength topography. For a more moderate rotational influence, fewer zonal jets form, Hadley-like circulation cells develop, and heat flux peaks near the equator. This regime is predicted for Europa and is possible for Titan, and may help drive geologic activity via thermocompositional diapirism in the ice shell. Weak rotational influence allows concentric zonal flows and overturning cells with no preferred orientation. Predictions for Ganymede’s ocean span all of these regimes.

Plain Language Summary: The outer solar system is host to a large number of diverse satellites, many of which likely have global oceans beneath their outer icy shells. I use theoretical arguments and numerical models to make predictions about ocean currents and heat transfer across such oceans. Our results suggest that strong ocean currents exist in Enceladus, Titan, Europa, and Ganymede, and cause the transfer of heat to vary with latitude that may modify the overlying ice shell.

1 Introduction

Exploration of the outer solar system has shown that subsurface oceans may be relatively common in the interiors of icy satellites and dwarf planets (Nimmo & Pappalardo, 2016; Lunine, 2017). Strong evidence exists for oceans in the Saturnian satellites Enceladus and Titan, with oceans also potentially present in Mimas and Dione. In the Jovian system, there is compelling evidence for a European ocean and oceans are predicted within Ganymede and potentially Callisto as well (c.f. Hartkorn & Saur, 2017). Kuiper belt objects, such as Pluto, Charon, and the Neptunian satellite Triton, may also have subsurface oceans.

The presence of liquid water makes these ocean worlds compelling astrobiological targets. However, the dynamics of these oceans also play a role in promoting habitable environments. For example, heat and material exchange between the seafloor and ice shell will be enhanced if the ocean is unstable to convection (e.g., Vance & Goodman, 2009; Soderlund et al., 2014) or has mechanically driven flows (e.g., Tyler, 2008; Lemasquerier et al., 2017; Wilson & Kerswell, 2018). Currents and turbulence tend to mix the ocean waters, which implies the presence of strong thermal and compositional gradients near the top and bottom of the ocean that life may take advantage of. Mixing efficiency may vary spatially, so these motions are also important for the distribution of potential bionutrients. In addition, heat transfer from the ocean will influence where the ice shell melts and freezes. Melting of the ice shell and freezing of the ocean will impact the salt budget, especially near the ice-ocean interface, a habitable environment in analogous terrestrial ice shelves (e.g., Daly et al., 2013). Moreover, accreted ice depleted in salts may have positive buoyancy and lead to upwelling thermocompositional diapirs in the ice shell that would link the surface and subsurface (e.g., Pappalardo & Barr, 2004; Soderlund et al., 2014).

Here, I focus on the ocean dynamics of Enceladus and Titan given the abundance of data from the Cassini mission and of Europa and Ganymede in preparation for the upcoming Europa Clipper (Phillips & Pappalardo, 2014) and JUICE (Grasset et al., 2013) missions. Scaling laws for rotating convection systems are used to make predictions about their convective behaviors in Section 2, and numerical models of global ocean convection characterizing the predicted regimes are presented in Section 3. Implications of these results are discussed in Section 4.

2 Rotating Convection Scaling Laws

Convection characteristics depend critically on the relative importance of rotation, which tends to organize the fluid into columns aligned with the rotation axis, increase the critical Rayleigh number, constrain heat transfer efficiency, and drive zonal flows (e.g., Aurnou et al., 2015). Cheng et al. (2018) combines asymptotic predictions, laboratory experiments, and numerical simulations to characterize the behavior of rotating thermal convection as a function of the dimensionless Ekman, Rayleigh, and Prandtl numbers. The Ekman number, $E = \nu/2\Omega D^2$, represents the ratio of rotational to viscous timescales; thus, low Ekman numbers signify rapid rotation rates in planetary interiors. The Rayleigh number, $Ra = \alpha g \Delta T D^3 / \nu \kappa$, is the ratio of the thermal diffusion time to the viscous buoyant rise time; large Rayleigh numbers denote strong buoyancy forcing. The Prandtl number, $Pr = \nu/\kappa$, defines the ratio of thermal to viscous diffusion timescales. Here, ν is kinematic viscosity, Ω is rotation rate, D is ocean thickness, α is thermal expansivity, g is gravitational acceleration, ΔT is superadiabatic temperature contrast, and κ is thermal diffusivity.

Cheng et al. (2018) identify five rotating convection regimes: columnar, plumes, geostrophic turbulence (GT), unbalanced boundary layer (UBL), and nonrotating heat transfer (NR) (see Fig. 1). Near onset, convection in the bulk fluid manifests as Taylor columns aligned with the rotation axis (“columnar” regime). With increased buoyancy forcing, the columns begin to deteriorate such that they no longer extend fully across the fluid layer (“plumes” regime). Convection eventually becomes vigorous enough for strong mixing in the bulk fluid (“geostrophic turbulence” regime). Despite the disappearance of coherent vertical structures, the Coriolis force still imposes a vertical stiffness on the flow field. These regimes are shown collectively on Figure 1. The influence of rotation is lost locally at Rayleigh numbers exceeding Ra_{GTU} , which corresponds to the breakdown of geostrophy (balance between Coriolis and pressure gradient forces) in the thermal boundary layers (“unbalanced boundary layers” regime). For Rayleigh numbers greater than Ra_{UNR} , the influence of rotation is lost globally (“nonrotating heat transfer” regime). Significant debate exists in the community on the scaling laws for Ra_{GTU} and Ra_{UNR} ; thus, I consider the bounding scalings highlighted by Cheng et al. (2018) for each.

Using this regime diagram, one can predict the convective regime of a system if the Ekman, Rayleigh, and Prandtl numbers can be estimated. The Prandtl number depends only on fluid properties and is estimated to be $Pr \approx 13$ assuming temperatures near the freezing point and terrestrial salinities (Melosh et al., 2004; Nayar et al., 2016). The Ekman number is also relatively easy to calculate since it only requires assumptions about the fluid viscosity, rotation rate, and ocean thickness (see Table 1). I use the internal structure models of Vance et al. (2018) to determine D and consider three possible ocean thickness values to represent the uncertainty at present as well as over the satellites’ evolutions. The nominal thickness is taken to be the average value of those predicted by their models (see Tables 5-8 of Vance et al. (2018)). As an upper limit, I consider the maximum combined liquid water-ice layer thicknesses of their models. The lower limit is assumed to be the minimum ocean thickness in their models or half of the nominal thickness, whichever is less. Enceladus has the largest nominal ocean Ekman number of $E \sim 2 \times 10^{-11}$, while the ocean of Ganymede has the lowest at $E \sim 1 \times 10^{-12}$.

The Rayleigh number is more difficult to estimate because it requires knowledge of the superadiabatic temperature contrast ΔT . One can derive an estimate, however, using the relationship between the Rayleigh number and the convective heat transfer efficiency as measured by the Nusselt number, $Nu = qD/\rho C_p \kappa \Delta T$. Following Soderlund et al. (2014), I leverage Nu – Ra scalings to solve for ΔT algebraically and consider both non-rotating and rapidly rotating scaling laws to give end-member estimates. More recent scaling laws for rotating spherical shells are used here, however. In the non-rotating regime, heat transfer is expected to be independent of the Ekman number and follow the

Table 1. Properties of icy satellite oceans in dimensional units and non-dimensional parameters. Fluid properties assume terrestrial seawater values, except for Titan’s density following Mitri et al. (2014). Ocean thickness and heat flux values (minimum, **nominal**, maximum) follow Vance et al. (2018). The Ekman number assumes the nominal ocean thickness; the temperature anomaly and Rayleigh number assume the given ranges of ocean thickness and heat flux values.

	Enceladus	Titan	Europa	Ganymede
Gravitational acceleration, g [m ² /s]	0.1	1.4	1.3	1.4
Density, ρ [kg/m ³]	1030	1200	1030	1030
Specific heat capacity, C_p [J/kg/K]	4000	4000	4000	4000
Thermal expansivity, α [K ⁻¹]	2×10^{-5}	2×10^{-5}	2×10^{-5}	2×10^{-5}
Thermal diffusivity, κ [m ² /s]	1.8×10^{-6}	1.8×10^{-6}	1.8×10^{-6}	1.8×10^{-6}
Kinematic viscosity, ν [m ² /s]	1.8×10^{-6}	1.8×10^{-6}	1.8×10^{-6}	1.8×10^{-6}
Rotation rate, Ω [s ⁻¹]	5.3×10^{-5}	4.6×10^{-6}	2.1×10^{-5}	1.0×10^{-5}
Ocean thickness, D [km]	10, 32 , 73	91, 285 , 540	57, 113 , 136	24, 300 , 930
Heat flux, q [mW/m ²]	1, 78 , 779	1, 11 , 109	8, 82 , 824	4, 38 , 375
Temperature anomaly, ΔT [mK]	1 – 171	0.05 – 19	0.4 – 96	0.1 – 51
Prandtl number, $Pr = \nu/\kappa$	13	13	13	13
Ekman number, $E = \nu/\Omega D^2$	2×10^{-11}	2×10^{-12}	3×10^{-12}	1×10^{-12}
Rayleigh number, $Ra = \alpha g \Delta T D^3 / \nu \kappa$	$10^{16} - 10^{21}$	$10^{18} - 10^{23}$	$10^{19} - 10^{22}$	$10^{17} - 10^{25}$

theoretical limit of $Nu = 0.07Ra^{1/3}$ (e.g., Gastine et al., 2015). Conversely, in the rapidly rotating limit, heat transfer is predicted to follow $Nu = 0.15Ra^{3/2}(2E)^2$ (Gastine et al., 2016). As a result, the temperature contrast is given by

$$\Delta T = 7.3 \left(\frac{\nu}{\alpha g \rho C_p} \right)^{1/4} q^{3/4} \quad (1)$$

in the non-rotating regime and by

$$\Delta T = 2.1 \left(\frac{\Omega^4 \kappa}{\rho^2 C_p^2 \nu \alpha^3 g^3} \right)^{1/5} (q^2 D)^{1/5} \quad (2)$$

in the rapidly-rotating regime. Here, I consider three ocean thicknesses (maximum, mean, minimum) as well as a range of heat flow values given their large uncertainties. As above, the nominal heat flux is set to the average value predicted by the Vance et al. (2018) models; the upper and lower bounds are assumed to be an order of magnitude larger and smaller. At Enceladus, I decrease the lower bound by another factor of six since the observed heat flux (Howett et al., 2011) is approximately sixty times greater than the radiogenic value (Chen et al., 2014). Temperature anomalies are found in the range of tenths to hundreds of milliKelvin. Rayleigh numbers span from $Ra \sim 10^{16}$ for the lower Enceladus limit to $Ra \sim 10^{25}$ for the upper Ganymede limit. An important caveat to note here, however, is that these estimates do not include compositional contributions due to salinity gradients. This simplification may be especially significant for Titan since the ocean is hypothesized to have a high concentration of dissolved salts (Baland et al., 2014; Mitri et al., 2014).

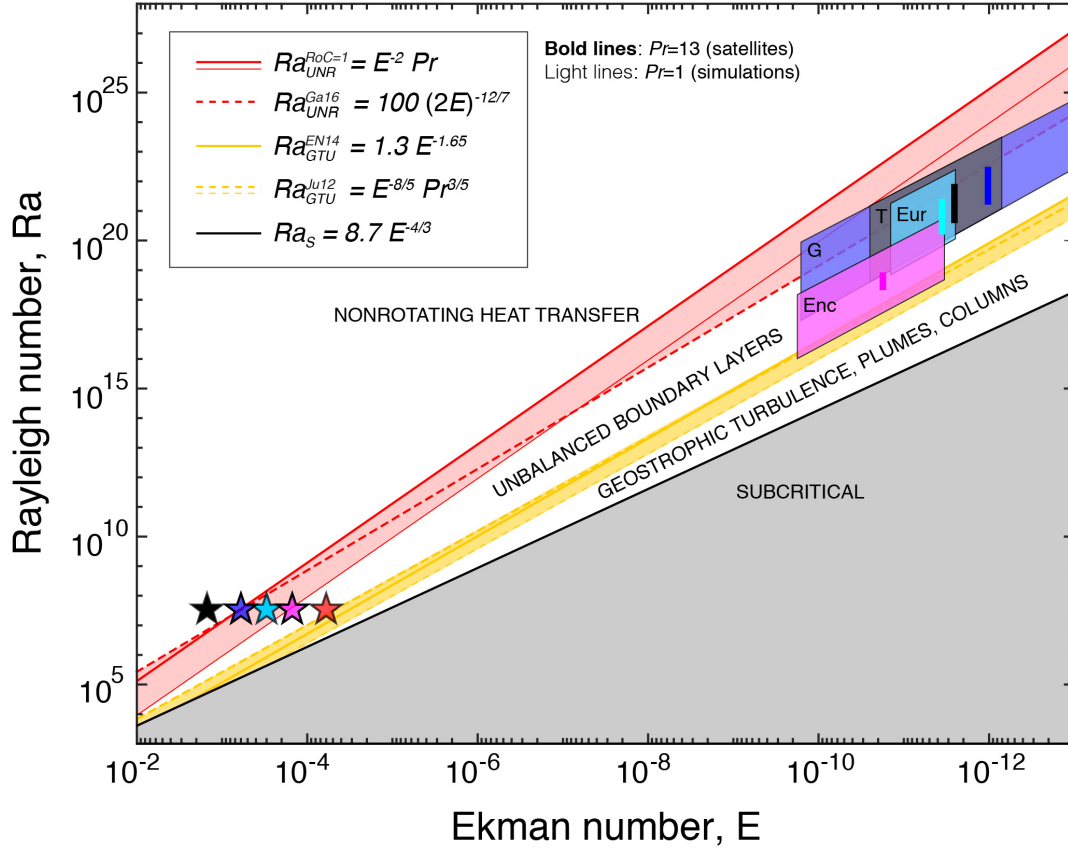


Figure 1. Convective regime diagram as defined by Cheng et al. (2018) with superimposed parameter estimates for Enceladus (magenta), Titan (gray), Europa (cyan), and Ganymede (blue) superimposed; boxes reflect uncertainties in heat flux and ocean thickness values and bold vertical lines represent their nominal estimates (see Table 1). Our numerical simulations are denoted by stars: red ($E = 3.0 \times 10^{-5}$), magenta ($E = 7.5 \times 10^{-5}$), cyan ($E = 1.5 \times 10^{-4}$), blue ($E = 3.0 \times 10^{-4}$), and black ($E = 7.5 \times 10^{-4}$). The solid black line denotes the scaling for the onset of convection (Chandrasekhar, 1961), the yellow lines bound the range of predicted transitions from the geostrophic turbulence regime to the unbalanced boundary layer regime (Ecke & Niemela, 2014; Julien et al., 2012), and the red lines bound the range of predicted transitions from the unbalanced boundary layer regime to the nonrotating heat transfer regime (Gastine et al., 2016; Gilman, 1977). The $Ra_{UNR}^{RoC=1}$ and Ra_{GTU}^{EN14} scalings depend on the Prandtl number, Pr ; bold lines assume $Pr = 13$ following estimates for icy satellite oceans while light lines assume $Pr = 1$ as used in the simulations.

Figure 1 plots the resulting estimates of the Ekman and Rayleigh numbers on the convective regime diagram defined by Cheng et al. (2018). The oceans of Titan, Europa, and Ganymede are predicted to behave similarly since their estimated parameter spaces have considerable overlap. Since these estimates fall near the lower boundary between the UBL and NR regimes, I hypothesize that rotational effects do not dominate the turbulent local-scale convective flows (c.f. Miquel et al., 2018). Conversely, rotation likely has a stronger influence on the ocean of Enceladus, which is also predicted to be primarily in the UBL regime, although extending into GT transition.

3 Numerical Convection Models

Numerical models of global ocean convection are next used to characterize the currents and heat flow patterns. I utilized the pseudospectral code MagIC, version 5.6 (e.g., Wicht, 2002; Gastine & Wicht, 2012) to simulate 3D, time-dependent, thermal convection of a Boussinesq fluid in a rotating spherical shell with geometry characterized by the ratio of inner to outer shell radii, $\chi = r_i/r_o = 0.9$. The system is further defined by the Ekman, Rayleigh, and Prandtl numbers. Following Soderlund et al. (2014), the boundaries are impenetrable, stress-free, and isothermal, and fluid motions derived from compositional buoyancy and orbital dynamics are neglected for simplicity.

Five cases that span a convective regime space consistent with the icy satellite ocean predictions (Fig. 1) are considered. The Rayleigh and Prandtl numbers are fixed to $Ra = 3.4 \times 10^7$ and $Pr = 1$, and the Ekman number is increased from $E = 3.0 \times 10^{-5}$ to $E = 7.5 \times 10^{-4}$. Hyperdiffusivities are not employed (c.f. Zhang & Schubert, 2000). The numerical grids have 73 radial points, 320 latitudinal points, and 640 longitudinal points for cases with $E \geq 7.5 \times 10^{-5}$ and 65 radial points, 640 latitudinal points, and 1280 longitudinal points for the $E = 3.0 \times 10^{-5}$ case. Each case was initiated with a random temperature perturbation or restarted from a lower Ekman number case.

Figure 2 shows the mean velocity fields of each model. In the lowest Ekman number case, Coriolis forces organize the flow into narrow radial structures that are aligned with the rotation axis. Reynolds stresses associated with these columns drive prograde equatorial flow with jets that alternate in direction at higher latitudes due to correlation locally between the azimuthal and cylindrically radial flow components (e.g., Aurnou & Olson, 2001; Christensen, 2001; Heimpel et al., 2005; Gastine et al., 2014). When the Ekman number is increased to $E = 7.5 \times 10^{-5}$, the system becomes increasingly turbulent and the convective flows lose some their axial coherence. The zonal flow pattern is relatively unchanged at high latitudes, but one less jet forms at large cylindrical radii, causing the equatorial jet to become retrograde. The mean radial flows become larger scale with a pronounced upwelling near the equator and downwellings at mid-latitudes, essentially forming Hadley-like meridional circulation cells in each hemisphere. The high latitude flows still retain some axialization, however. Further increasing the Ekman number ($1.5 \times 10^{-4} \leq E \leq 3.0 \times 10^{-4}$) reduces the influence of the Coriolis force sufficiently to allow mixing of absolute angular momentum (e.g., Gilman, 1978; Aurnou et al., 2007; Gastine et al., 2013). As a result, zonal flows are retrograde at large cylindrical radii and prograde closer to the rotation axis. The width of the equatorial upwelling also broadens and loses alignment with the rotation axis. Both mean zonal and radial flow speeds increase by a factor of five compared to the $E = 7.5 \times 10^{-5}$ case. In the highest Ekman number case, the zonal and radial flows have comparable magnitudes reminiscent of non-rotating convection. The radial flows have no preferred spatial orientation, while the zonal flows become increasingly concentric rather than vertical due to the increased role of viscous transport of angular momentum (Brun & Palacios, 2009).

These velocity field changes lead to distinct changes in heat flow patterns. Figure 3 shows the mean radial temperature gradient along the outer boundary. In the lowest Ekman number case, heat flow peaks at high latitudes with minima near the equator due

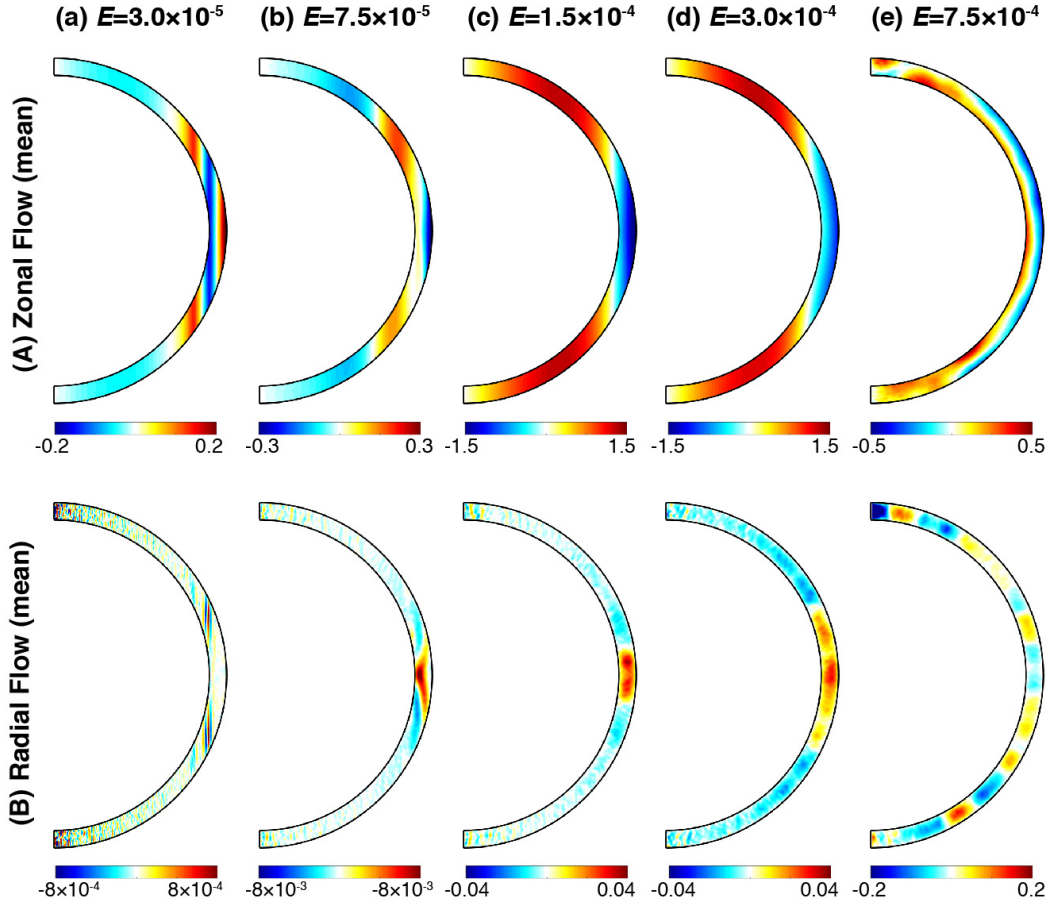


Figure 2. Velocity fields averaged over all longitudes and at least 0.02 viscous diffusion times for each model (columns a-e). (A) Zonal flows given in dimensionless Rossby number units, $Ro = U/\Omega D$, which characterizes the ratio of rotational to inertial timescales. Red (blue) denotes prograde (retrograde) currents. (B) Radial flows given in Ro units. Red (blue) denotes upwelling (downwelling) currents.

to the axialization of convective flow structures and development of the strong equatorial jet (e.g., Aurnou et al., 2008). At intermediate Ekman numbers, formation of the Hadley-like circulation cells enhance low latitude heat flux with minima at mid-latitudes. Secondary peaks are found at high latitudes due to turbulent heat transfer associated with vertically ascending plumes. In the highest Ekman number case, the heat flow pattern reflects the development of multiple circulation cells that drift over time. The degree of mixing within the interior is reflected by the $\partial T/\partial r$ amplitude, with larger values denoting a more isothermalized interior and thinner thermal boundary layers.

4 Discussion

In order to apply these models to icy satellite oceans, I assume that the velocity and temperature patterns extrapolate to more extreme parameters following the relative distance between regime boundaries. Enceladus' ocean may then be represented by the $E = [3.0 \times 10^{-5}, 7.5 \times 10^{-5}]$ models since both fall approximately between the GT-UBL regime transition and the lower bound of the UBL-NR transition. In contrast, the oceans of Europa, Ganymede, and Titan depend on the UBL-NR transition scaling used.

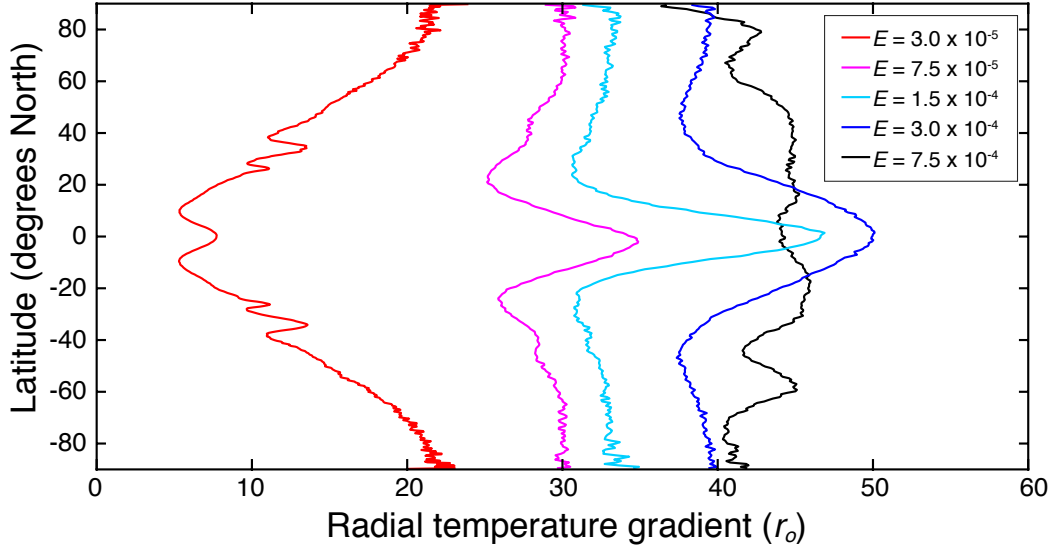


Figure 3. Dimensionless radial temperature gradient $\partial T/\partial r$ along the outer boundary averaged over all longitudes and at least 0.02 viscous diffusion times. Cases are denoted by color.

If $Ra_{UNR}^{RoC=1} = E^{-2}Pr$ (e.g., Gilman, 1977) is assumed, then all of these oceans are near the center of UBL regime such that the $E = [3.0 \times 10^{-5}, 7.5 \times 10^{-5}]$ models would again be most appropriate. If the transition instead follows $Ra_{UNR}^{Ga16} = 100(2E)^{-12/7}$ (Gastine et al., 2016), then the $E = [1.5 \times 10^{-4}, 7.5 \times 10^{-4}]$ models would be most pertinent, with nominal parameter estimates best represented by the $E = 1.5 \times 10^{-4}$ model.

Below, I discuss the implications for each satellite and look ahead to future missions. This analysis focuses on the heat flux pattern along the ice-ocean interface (i.e. $\partial T/\partial r|_{r=r_o}$). Regions with high heat flow are presumed to undergo enhanced melting, leading to ice shell thickness variations. However, large thickness disparities can set up a phenomena known as an ice pump (e.g., Lewis & Perkin, 1986) where pressure-induced melting occurs where the ice shell is thick and re-accretes where the ice shell is thin, effectively reducing topography along the base of the ice shell. Since the accretion process is very efficient at excluding impurities in low temperature environments (e.g., Moore et al., 1994; Eicken et al., 1984), this marine ice may be salt-depleted compared to the overlying ice. The ice may, therefore, have positive buoyancy due to the associated thermal and compositional density anomalies and rise toward the surface in the form of convective diapirs (e.g., Pappalardo & Barr, 2004; Soderlund et al., 2014). Alternatively, if the ice pump mechanism is not efficient, the ice shell may be more unstable to convection where it is relatively thick (Goodman, 2014).

For Enceladus, I predict the zonal flows to be characterized by multiple jets that alternate in direction (Fig. 2A a,b). Converting model velocities to dimensional units $U = \Omega DR_o$, I expect peak zonal speeds of approximately 0.5 m/s. Meridional circulations are predicted to either be strongly aligned with the rotation axis with speeds up to a cm/s (Fig. 2B a) or to be concentrated in a low latitude upwelling with speeds up to a few cm/s (Fig. 2B b). Instantaneous velocities can locally be an order of magnitude larger for all models. As a result, heat flow along the ice-ocean interface has distinct peaks at either the poles (Fig. 3, red line) or at the equator and the poles secondarily (Fig. 3, magenta line).

Measurements of Enceladus’ gravitational field and librational motions show that the ice shell is thin below the south pole and thick at the equator, with an intermediate thickness at the north pole (Čadek et al., 2016; Beuthe et al., 2016). Inverting these measurements to infer the ocean heat flux along the ice-ocean interface, Čadek et al. (2019) find peak flux near the poles with a minima at the equator. These observations are consistent with the heat flux distribution of the $E = 3.0 \times 10^{-5}$ model (Fig. 3), which is the appropriate analog if a low internal heat flux is assumed (Fig. 1).

Given the similarities in regime predictions for Titan, Europa, and Ganymede, they are considered together here. Assuming the nominal model and the Ra_{UNR}^{Ga16} scaling, these satellites are predicted to have three zonal jets with retrograde flow outside the tangent cylinder (imaginary right cylinder aligned with the rotation axis and tangent to the seafloor) and prograde flow at higher latitudes (Fig. 2A c). Jet speeds reach $\sim [2, 4, 5]$ m/s for [Titan, Europa, Ganymede], respectively. The local convective motions are fast (order m/s) and not strongly constrained by rotation; on average, they organize to form an equatorial upwelling with peak speeds of $\sim [5, 9, 12]$ cm/s (Fig. 2B c). Heat flow along the ice-ocean interface is maximum near the equator, with secondary maxima near the poles (Fig. 3, cyan line). Alternatively, for the $Ra_{UNR}^{RoC=1} = E^{-2}Pr$ scaling, these satellites are predicted to behave similarly to Enceladus as discussed above, except with respect to dimensionalized flow speeds that will be a factor of $\sim [0.8, 1.4, 1.7]$ times faster.

Looking to Titan, the satellite’s surface topography shows polar depressions compared to relatively elevated low latitudes (Nimmo & Bills, 2010; Choukroun & Sotin, 2012; Kvorka et al., 2018). The three intermediate Titan-relevant models have peak heat fluxes near the equator (Fig. 3, magenta, cyan, and blue lines). These peaks are significantly stronger than the secondary enhancements at high latitudes such that melting would cause the equator to be relatively thin compared to the poles, opposite to the observations. If this region were infilled with relatively pure marine ice, however, an equatorial bulge may result through Pratt isostasy. Associated thermocompositional diapirism could potentially lead to cryovolcanism that appears to be concentrated at low latitudes (e.g., Sohl et al., 2014). Alternatively, the lowest Ekman number model may be appropriate if we assume the $Ra_{UNR}^{RoC=1} = E^{-2}Pr$ scaling and/or if a stable salinity gradient reduces the effective buoyancy forcing of the ocean (Ra). High oceanic heat flux and associated melting at high latitudes would then be consistent with the polar depression through Airy isostasy (Kvorka et al., 2018).

Europa has a young, tortured surface with geologic features indicating recent activity and the potential for ocean-derived materials (e.g., Figueredo & Greeley, 2003; Fischer et al., 2015). These chaos terrains appear to be located preferentially at low latitudes with a secondary prevalence near the poles (Leonard et al., 2018), and formation models suggest that they may be associated with upwelling diapirs (e.g., Collins & Nimmo, 2009; Schmidt et al., 2011) and marine ice accretion (Soderlund et al., 2014). No large gradients in ice shell thickness have been detected (Nimmo et al., 2007), suggesting an efficient ice pump (c.f. Nimmo, 2004). Given that most Europa-relevant models predict high oceanic heat flux at low latitudes with relatively low flux at mid-latitudes (Fig. 3, magenta, cyan, and blue lines), our new calculations continue to support the thermocompositional diapirism hypothesis.

The observational constraints for Ganymede are much more limited. The satellite’s ancient grooved terrains indicate a likely period of geologic activity in its early history (Lucchita, 1980) and detection of hydrated salts suggests a subsurface briny layer of fluid (McCord et al., 2001), but no clear patterns are present. Mass anomalies were measured in the northern hemisphere during a single Galileo flyby (Palguta et al., 2006), but the sparsity of data prohibit both characterization on a global scale and unique determination of their depth of origin. Consequently, there is no clear link at present between observations and the underlying ocean dynamics.

Future missions to the outer solar system may be able to better constrain the ocean flows and test the predictions of our calculations and convection models. Looking specifically to the Jovian system, the Europa Clipper and JUICE missions will determine the ocean thickness and salinity and may be able to place constraints on spatial variations of ice shell thickness (e.g., Phillips & Pappalardo, 2014; Grasset et al., 2013). Ice penetrating radar will provide information on ice shell thermophysical structure and constrain ice-ocean exchange processes (e.g., Kalousová et al., 2017), while magnetometer measurements may allow probing of ocean currents through their induction of magnetic fields (e.g., Tyler, 2011).

Acknowledgments

I thank Jonathan Aurnou for his helpful comments. This work was supported by NASA Grant NNX14AR28G. Computational resources were provided by the NASA High-End Computing (HEC) Program through the NASA Advanced Supercomputing (NAS) Division at Ames Research Center. The MagIC code is publicly available at <https://magic-sph.github.io/contents.html>. All data is provided within the publication pages.

References

- Aurnou, J. M., Calkins, M. A., Cheng, J. S., Julien, K., King, E. M., Nieves, D., . . . Stellmach, S. (2015). Rotating convective turbulence in earth and planetary cores. *Phys. Earth Planet. Int.*, *246*, 52–71.
- Aurnou, J. M., Heimpel, M. H., Allen, L., King, E. M., & Wicht, J. (2008). Convective heat transfer and the pattern of thermal emission on the gas giants. *Geophys. J. Int.*, *173*, 793–801.
- Aurnou, J. M., Heimpel, M. H., & Wicht, J. (2007). The effects of vigorous mixing in a convective model of zonal flow on the Ice Giants. *Icarus*, *190*, 110–126.
- Aurnou, J. M., & Olson, P. L. (2001). Strong zonal winds from thermal convection in a rotating spherical shell. *Geophys. Res. Lett.*, *28*(13), 2557–2559.
- Baland, R.-M., Tobie, G., Lefevre, A., & Van Hoolst, T. (2014). Titan’s internal structure inferred from its gravity field, shape, and rotation state. *Icarus*, *237*, 29–41.
- Beuthe, M., Rivoldini, A., & Trinh, A. (2016). Enceladus’s and Dione’s floating ice shells supported by minimum stress isostasy. *Geophys. Res. Lett.*, *43*(19).
- Brun, A. S., & Palacios, A. (2009). Numerical simulations of a rotating red giant star. I. Three-dimensional models of turbulent convection and associated mean flows. *Astrophys. J.*, *702*, 1078–1097.
- Čadek, O., Souček, O., Běhouňková, M., Choblet, G., Tobie, G., & Hron, J. (2019). Long-term stability of Enceladus’ uneven ice shell. *Icarus*, *319*, 476–484.
- Čadek, O., Tobie, G., Van Hoolst, T., Massé, M., Choblet, G., Lefèvre, A., . . . others (2016). Enceladus’s internal ocean and ice shell constrained from Cassini gravity, shape, and libration data. *Geophys. Res. Lett.*, *43*(11), 5653–5660.
- Chandrasekhar, S. (1961). *Hydrodynamic and hydromagnetic stability*. Oxford: Clarendon.
- Chen, E., Nimmo, F., & Glatzmaier, G. A. (2014). Tidal heating in icy satellite oceans. *Icarus*, *229*, 11–30.
- Cheng, J. S., Aurnou, J. M., Julien, K., & Kunnen, R. P. J. (2018). A heuristic framework for next-generation models of geostrophic convective turbulence. *Geophys. Astrophys. Fluid Dyn.*, *112*(4), 277–300.
- Choukroun, M., & Sotin, C. (2012). Is Titan’s shape caused by its meteorology and carbon cycle? *Geophys. Res. Lett.*, *39*(4).
- Christensen, U. R. (2001). Zonal flow driven by deep convection on the major planets. *Geophys. Res. Lett.*, *28*, 2553–2556.

- Collins, G., & Nimmo, F. (2009). Chaotic terrain on Europa. In R. T. Pappalardo, W. B. McKinnon, & K. K. Khurana (Eds.), *Europa* (p. 259-281). Tucson: University of Arizona Press.
- Daly, M., Rack, F., & Zook, R. (2013). *Edwardsiella andrillae*, a new species of sea anemone from Antarctic Ice. *PloS one*, 8(12), e83476.
- Ecke, R. E., & Niemela, J. J. (2014). Heat transport in the geostrophic regime of rotating Rayleigh-Bénard convection. *Phys. Rev. Lett.*, 113, 114301.
- Eicken, H., Oerter, H., Miller, H., & Graf, W. (1984). Textural characteristics and impurity content of meteoric and marine ice in the Ronne Ice Shelf, Antarctica. *J. Glaciol.*, 40(135), 386–398.
- Figueredo, P. H., & Greeley, R. (2003). The Emerging Resurfacing History of Europa from Pole-to-Pole Geologic Mapping. In Mackwell, S. and Stansbery, E. (Ed.), *Lunar and Planetary Institute Science Conference Abstracts* (Vol. 34, p. 1017).
- Fischer, P. D., Brown, M. E., & Hand, K. P. (2015). Spatially resolved spectroscopy of Europa: The distinct spectrum of large-scale chaos. *Astron. J.*, 150(5), 164.
- Gastine, T., Heimpel, M. H., & Wicht, J. (2014). Zonal flow scaling in rapidly-rotating compressible convection. *Phys. Earth Planet. Int.*, 232, 36–50.
- Gastine, T., & Wicht, J. (2012). Effects of compressibility on driving zonal flow in gas giants. *Icarus*, 219, 428–442.
- Gastine, T., Wicht, J., & Aubert, J. (2016). Scaling regimes in spherical shell rotating convection. *J. Fluid Mech.*, 808, 690–732.
- Gastine, T., Wicht, J., & Aurnou, J. M. (2013). Zonal flow regimes in rotating anelastic spherical shells: An application to giant planets. *Icarus*, 225, 156–172.
- Gastine, T., Wicht, J., & Aurnou, J. M. (2015). Turbulent Rayleigh-Bénard convection in spherical shells. *J. Fluid Mech.*, 778, 721–764.
- Gilman, P. A. (1977). Nonlinear dynamics of Boussinesq convection in a deep rotating spherical shell – I. *Geophys. Astrophys. Fluid Dyn.*, 8, 93–135.
- Gilman, P. A. (1978). Nonlinear dynamics of Boussinesq convection in a deep rotating spherical shell – II. *Geophys. Astrophys. Fluid Dyn.*, 11, 157–179.
- Goodman, J. C. (2014). Flow of an alien ocean. *Nature Geosci.*, 7, 8–9.
- Grasset, O., Dougherty, M. K., Coustenis, A., Bunce, E. J., Erd, C., Titov, D., ... others (2013). Jupiter ICy moons Explorer (JUICE): An ESA mission to orbit Ganymede and to characterise the Jupiter system. *Planet. Space Sci.*, 78, 1–21.
- Hartkorn, O., & Saur, J. (2017). Induction signals from Callisto’s ionosphere and their implications on a possible subsurface ocean. *J. Geophys. Res.*, 122(11).
- Heimpel, M. H., Aurnou, J. M., & Wicht, J. (2005). Simulation of equatorial and high-latitude jets on Jupiter in a deep convection model. *Nature*, 433, 193–196.
- Howett, C. J. A., Spencer, J. R., Pearl, J. C., & Segura, M. (2011). High heat flow from Enceladus’ south polar region measured using 10–600 cm-1 Cassini/CIRS data. *J. Geophys. Res.*, 116(E3).
- Julien, K., Knobloch, E., Rubio, A. M., & Vasil, G. M. (2012). Heat transport in low-Rossby-number Rayleigh-Bénard convection. *Phys. Rev. Lett.*, 109, 254503.
- Kalousová, K., Schroeder, D. M., & Soderlund, K. M. (2017). Radar attenuation in Europa’s ice shell: Obstacles and opportunities for constraining the shell thickness and its thermal structure. *J. Geophys. Res. Planets*, 122(3), 524–545.
- Kvorka, J., Cadek, C., Tobie, G., & Choblet, G. (2018). Does Titan’s long-wavelength topography contain information about subsurface ocean dynamics? *Icarus*, 310, 149–164.
- Lemasquerier, D., Grannan, A. M., Vidal, J., Cébron, D., Favier, B., Le Bars, M., & Aurnou, J. M. (2017). Libration-driven flows in ellipsoidal shells. *J. Geophys. Res. Planets*, 122(9), 1926–1950.
- Leonard, E. J., Patthoff, D. A., Senske, D. A., & Collins, G. C. (2018). The Europa Global Geologic Map. *LPI Contributions*, 2066.

- Lewis, E. L., & Perkin, R. G. (1986). Ice pumps and their rates. *J. Geophys. Res.*, *91*, 11756–11762.
- Lucchita, B. K. (1980). Grooved terrain on Ganymede. *Icarus*, *44*(2), 481–501.
- Lunine, J. I. (2017). Ocean worlds exploration. *Acta Astronautica*, *131*, 123–130.
- McCord, T. B., Hansen, G. B., & Hibbitts, C. A. (2001). Hydrated salt minerals on Ganymede’s surface: evidence of an ocean below. *Science*, *292*(5521), 1523–1525.
- Melosh, H. J., Ekholm, A. G., Showman, A. P., & Lorenz, R. D. (2004). The temperature of Europa’s subsurface water ocean. *Icarus*, *168*, 498–502.
- Miquel, B., Xie, J.-H., Featherstone, N., Julien, K., & Knobloch, E. (2018). Equatorially trapped convection in a rapidly rotating shallow shell. *Phys. Rev. Fluids*, *3*(5), 053801.
- Mitri, G., Meriggiola, R., Hayes, A., Lefevre, A., Tobie, G., Genova, A., ... Zebker, H. (2014). Shape, topography, gravity anomalies and tidal deformation of Titan. *Icarus*, *236*, 169–177.
- Moore, J. C., Reid, A. P., & Kipfstuhl, J. (1994). Microphysical and electrical properties of marine ice and its relationship to meteoric and sea ice. *J. Geophys. Res.*, *99*, 5171–5180.
- Nayar, K. G., Sharqawy, M. H., & Banchik, L. D. (2016). Thermophysical properties of seawater: a review and new correlations that include pressure dependence. *Desalination*, *390*, 1–24.
- Nimmo, F. (2004). Non-newtonian topographic relaxation on Europa. *Icarus*, *168*, 205–208.
- Nimmo, F., & Bills, B. G. (2010). Shell thickness variations and the long-wavelength topography of Titan. *Icarus*, *208*(2), 896–904.
- Nimmo, F., & Pappalardo, R. T. (2016). Ocean worlds in the outer solar system. *J. Geophys. Res. Planets*, *121*(8), 1378–1399.
- Nimmo, F., Thomas, P. C., Pappalardo, R. T., & Moore, W. B. (2007). The global shape of Europa: Constraints on lateral shell thickness variations. *Icarus*, *191*, 183–192.
- Palguta, J., Anderson, J. D., Schubert, G., & Moore, W. B. (2006). Mass anomalies on Ganymede. *Icarus*, *180*, 428–441.
- Pappalardo, R. T., & Barr, A. C. (2004). The origin of domes on Europa: The role of thermally induced compositional diapirism. *Geophys. Res. Lett.*, *31*, L01701.
- Phillips, C. B., & Pappalardo, R. T. (2014). Europa Clipper mission concept: Exploring Jupiter’s ocean moon. *Eos, Transactions American Geophysical Union*, *95*(20), 165–167.
- Schmidt, B. E., Blankenship, D. D., Patterson, G. W., & Schenk, P. M. (2011). Active formation of chaos terrain over shallow subsurface water on Europa. *Nature*, *479*, 502–505.
- Soderlund, K. M., Schmidt, B. E., Wicht, J., & Blankenship, D. D. (2014). Ocean-driven heating of Europa’s icy shell at low latitudes. *Nature Geoscience*, *7*, 16–19.
- Sohl, F., Solomonidou, A., Wagner, F. W., Coustenis, A., Hussmann, H., & Schulze-Makuch, D. (2014). Structural and tidal models of Titan and interferences on cryovolcanism. *J. Geophys. Res. Planets*, *119*(5), 1013–1036.
- Tyler, R. H. (2008). Strong ocean tidal flow and heating on moons of the outer planets. *Nature*, *456*, 770–773.
- Tyler, R. H. (2011). Magnetic remote sensing of Europa’s ocean tides. *Icarus*, *211*, 906–908.
- Vance, S., & Goodman, J. C. (2009). Oceanography of an ice-covered moon. In R. T. Pappalardo, W. B. McKinnon, & K. K. Khurana (Eds.), *Europa* (p. 459–482). Tucson: University of Arizona Press.
- Vance, S., Panning, M. P., Stahler, S., Cammarano, F., Bills, B. G., Tobie, G., ... Banerdt, B. (2018). Geophysical investigations of habitability in ice-covered ocean worlds. *J. Geophys. Res.*, *123*, 180–205.

- Wicht, J. (2002). Inner-core conductivity in numerical dynamo simulations. *Phys. Earth Planet. Int.*, *132*, 281–302.
- Wilson, A., & Kerswell, R. R. (2018). Can libration maintain Enceladus’s ocean? *Earth Planet. Sci. Lett.*, *500*, 41–46.
- Zhang, K., & Schubert, G. (2000). Magnetohydrodynamics in rapidly rotating spherical systems. *Annu. Rev. Fluid Mech.*, *32*, 409–443.